ARL-TR-9905 ● APR 2024

Effects of Strain-Rate and Cobalt Content on the Deformation and Failure of WC–xCo under Compression

by Tusit Weerasooriya, Paul Moy, and Weinong Chen

NOTICES

Disclaimers

ARL-TR-9905 ● APR 2024

Effects of Strain-Rate and Cobalt Content on the Deformation and Failure of WC–xCo under Compression

Tusit Weerasooriya and Paul Moy
DEVCOM Army Research Laboratory

Weinong Chen
Purdue University

REPORT DOCUMENTATION PAGE

1. REPORT DATE	2. REPORT TYPE	3. DATES COVERED — START DATE	3. DATES COVERED — END DATE
April 2024	Technical Report	January 2003	December 2004

4. TITLE AND SUBTITLE
Effects of Strain-Rate and Cobalt Content on the Deformation and Failure of WC–xCo under Compression

5a. CONTRACT NUMBER	5b. GRANT NUMBER	5c. PROGRAM ELEMENT NUMBER
5d. PROJECT NUMBER	**5e. TASK NUMBER**	**5f. WORK UNIT NUMBER**

6. AUTHOR(S)
Tusit Weerasooriya, Paul Moy, and Weinong Chen

7. PERFORMING ORGANIZATION NAME(S) AND ADDRESS(ES)	8. PERFORMING ORGANIZATION REPORT NUMBER
DEVCOM Army Research Laboratory ATTN: FCDD-RLA-TB Aberdeen Proving Ground, MD 21005	ARL-TR-9905

9. SPONSORING/MONITORING AGENCY NAME(S) AND ADDRESS(ES)	10. SPONSOR/MONITOR'S ACRONYM(S)	11. SPONSOR/MONITOR'S REPORT NUMBER(S)

12. DISTRIBUTION/AVAILABILITY STATEMENT
DISTRIBUTION STATEMENT A. Approved for public release: distribution unlimited.

13. SUPPLEMENTARY NOTES
ORCID ID: Tusit Weerasooriya, 0000-0003-3299-2166

14. ABSTRACT
The quasi-static, intermediate, and dynamic compressive responses of tungsten-carbide cermets alloyed with approximately 12 wt% and 6 wt% cobalt (Co) have been determined as a function of loading rates. To determine the dynamic properties, a modified split-Hopkinson pressure bar is used with wave shaping and a spherical joint. A similar spherical joint also is used in the quasi-static and intermediate rate experiments to minimize stress concentrations in the specimen through precise alignment loading. The compressive stress–strain response of the cermets is slightly nonlinear for both approximately 12 wt% and 6 wt% Co materials, and nonlinearity increases with the increase in Co content. Compressive strength increases with the strain rate for 12 wt% Co (from 4.5 GPa at quasi-static to 4.9 GPa at dynamic rates). Failure stress initially increases with strain rate for 6 wt% Co material (from 4.8 GPa at quasi-static to 5.1 GPa for intermediate [1/s] rates), but then decreases to 4.6 GPa at higher rates. The rate dependency of the failure stress is described by two models. In addition, carefully designed recovery experiments were executed to evaluate the evolution of microstructural damage during high-rate loading. Micrographs indicate that the crack propagation process is predominately intergranular.

15. SUBJECT TERMS
tungsten carbide–cobalt, cermets, dynamic response, failure behavior, function of cobalt, high-rate experimentation, ceramic response, Sciences of Extreme Materials, Terminal Effects, Weapons Sciences

16. SECURITY CLASSIFICATION OF: a. REPORT	b. ABSTRACT	C. THIS PAGE	17. LIMITATION OF ABSTRACT	18. NUMBER OF PAGES
UNCLASSIFIED	UNCLASSIFIED	UNCLASSIFIED	SAR	36

19a. NAME OF RESPONSIBLE PERSON	19b. PHONE NUMBER *(Include area code)*
Tusit Weerasooriya	(410) 306-0969

STANDARD FORM 298 (REV. 5/2020)
Prescribed by ANSI Std. Z39.18

Contents

List of Figures

List of Tables

1. Introduction

High-density ceramics are of special interest for a wide range of applications. Although many ceramic oxides, nitrides, carbides, and borides may be classified as high-density ceramics (Schneider 1991), most are either very difficult to process in a mass-production scale or are too expensive to be used as materials in engineering applications. Tungsten carbide (WC), which has one of highest densities and highest elastic moduli in this class of materials, can be processed industrially at acceptable costs and therefore recently attracted defense research interest (Gooch et al. 2000; Peron 2002). In commercial applications, titanium carbon nitrite coatings on base WC–cobalt (Co) tools increased hardness and decreased friction on the tool surface so dry-machining could be possible (Peng et al. 2005).

To reduce the pressure and temperature necessary in processing to facilitate mass production, base WC materials are alloyed mostly with Co. This composite is referred to as WC–xCo, where "x" indicates the percentage of the total weight of the composite that is due to the Co additive. Co is used as a binder in small quantities so the combined WC–xCo composite still maintains its strength characteristics. Co is added to WC powder to promote liquid phase sintering. The agglomerated powder can then be densified fully by isostatic compression and sintered at a lower pressure and lower temperature when compared with those necessary to sinter a pure WC ceramic. The processes of cold compaction and solid-state sintering of WC–xCo were studied and modeled (Favrot et al. 1999). While the introduction of the Co phase significantly improved the feasibility for the mass production of WC cermets, the effects of the metal phase on the mechanical behavior of the resultant cermets must be thoroughly understood before these materials can be used in practical engineering designs.

In processing, the addition of vanadium carbide during the sintering of WC–xCo inhibited grain growth and changed crystal shape (Lee et al. 2003). The grain size and the amount of Co in cermet material are identified as affecting ballistic performance of the ceramic armor materials (Gooch et al. 2000). More systematic characterization of material behavior of the cermets as a function of loading rates, WC grain size, and the amount of Co binder phase still needs to be carried out. There is evidence in the literature that compressive strength of WC–xCo cermets increases as strain rate increases (Cutler 1984).

This research follows our previous work on WC–12Co (Weerasooriya et al. 2004) and focuses on compressive stress–strain behavior (both deformation and failure) of WC cermets with similar WC grain-size distribution but different amounts of Co binder (~12 wt% and 6 wt% as well as no wt% Co, referred to hereafter as WC–

12Co, WC–6Co, and WC–0Co, respectively) are determined as a function of loading rates from quasi-static moderately high rate (HR). Specimens with WC–0Co had much greater variability and therefore are presented only in the Appendix of this report.

2. Material, Specimens, and Experiments

2.1 Material

The cermets with approximately 12 wt% and 6 wt% Co were received as rods with unknown chemistries (more details of the source for materials are in the Addendum Report ARL-TN-1196). Actual chemical compositions of the cermets were obtained through an external laboratory. The specimen material is a WC alloyed with approximately 12 wt% and 6 wt% Co (both materials also are identified as WC–xCo in this report). Elastic properties of these materials were measured using ultrasonic pulse-echo method (Alexander and Weerasooriya 2021). Due to the smaller size of the specimens, the measured elastic properties are scattered and show some variability. The WC–12Co and WC–6Co materials have mass densities of 14,395 and 14,729 kg/m^3, respectively. Actual chemical compositions, measured densities, average elastic properties, and sound velocities for both materials are presented in Table 1. Figure 1 shows the scanning electron microscope (SEM) micrographs of the WC–xCo cermets. Grain size distribution of the two cermets is approximately similar.

Table 1 Measured chemical composition, elastic properties, and densities of WC–12Co and WC–6Co

	WC–12Co	**WC–6Co**
WC (wt%)	88.4	93.3
Co (wt%)	11.6	6.7
Density (kg/m^3)	14,395	14,729
Long velocity (m/s)	6743	6927
Shear velocity (m/s)	3938	4179
Young’s modulus (GPa)	554	624
Shear modulus (GPa)	224	257
Poisson’s ratio	0.240	0.214

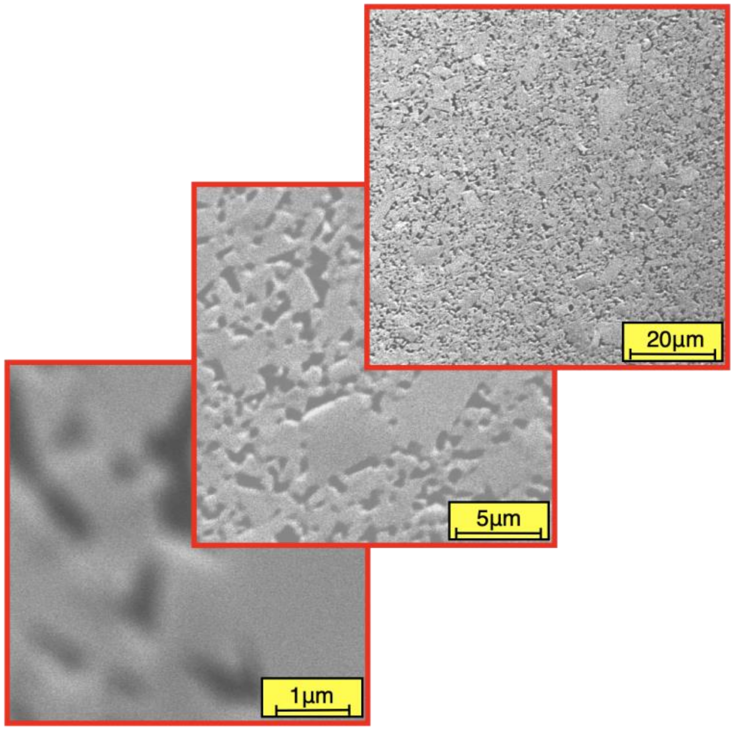

(a)

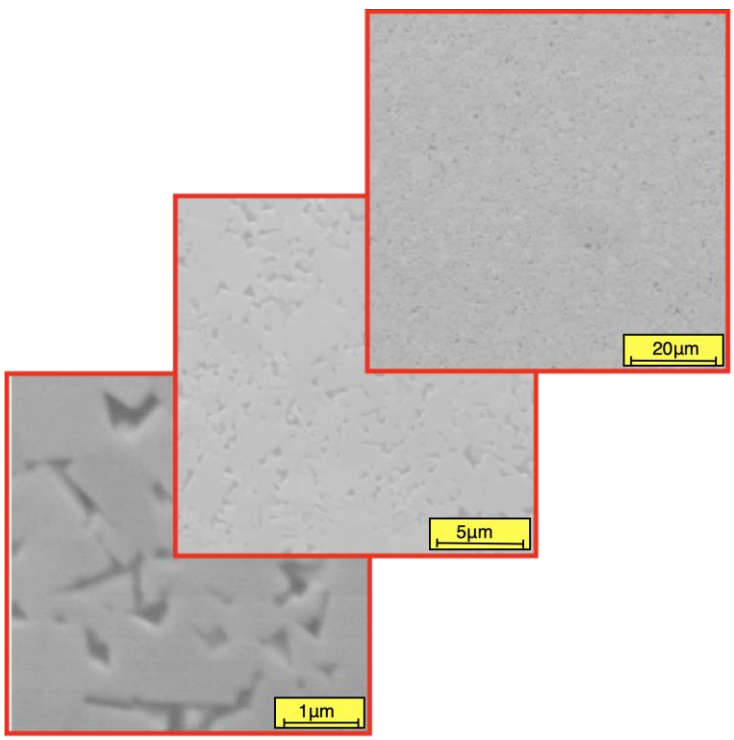

(b)

Fig. 1 SEM micrographs of WC–xCo cermets microstructure (more details of the materials are in the Addendum: ARL-TN-1196) being investigated. (a) WC–12Co and (b) WC–6Co.

2.2 Specimens

The material for test specimens was received as 5.59-mm (0.22-inch)-diameter rods. The rods were segmented into right cylindrical geometry of 5.59 mm in diameter and 5.59 mm in height. Both ends of the specimen were grounded flat and parallel to within 0.0005 mm and lapped to a mirror finish. A pair of strain gages were bonded on the cylindrical surface of the cermet specimen along the axial direction and 180° apart to record the transient strain history in the specimen during both low rates (LRs) and dynamic experiments. In addition, the pair of strain measurements provide insight on the validity for each alignment in the experiments. The specimen dimensions are the same for all experiments in this report.

2.3 HR Experimental Method

A modified split-Hopkinson pressure bar (SHPB) was employed in conducting dynamic compressive experiments. The striker, incident, and transmission bars used in this research are maraging steel bars of 89, 1524, and 1219 mm long, respectively, with a common diameter of 25.4 mm. The setup allowed for a nominal strain rate of 200/s.

SHPB, originally developed by Kolsky (1949) to provide dynamic stress–strain curves as a function of strain rates, has been used widely for metallic materials for almost half a century (Gray 2000; Chen and Song 2011). It also has been modified in the last few decades to determine the dynamic properties of other classes of engineering and soft materials (biological and polymeric), such as composites (Song et al. 2003), concrete (Anton and Subhash 2000), single-fibers (Cheng et al. 2004), biological soft tissues (Song et al. 2007; Cheng et al. 2009), bones (Sanborn et al. 2016; Weerasooriya et al. 2016; Brown et al. 2021), hard polymers (Moy et al. 2011), and ceramics (Ross et al. 1996; Chen and Ravichandran 1996, 1997; Luo and Chen 2004). To achieve valid dynamic testing conditions in dynamic experiments, loading pulse control in split-Hopkinson torsion, compression, and tension bars have been explored for more than three decades (Duffy et al. 1971; Nemat-Nasser et al. 1991). The details of SHPB and its working principle are well-described in literature and handbooks (Gray 2000).

This work briefly describes two modifications we employed on an SHPB to conduct valid dynamic experiments on the hard cermets investigated herein. The first modification is to control the shape of the loading pulse to achieve constant strain-rate dynamic equilibrium in the specimen that mechanically behaves slightly nonlinearly. The second modification is to ensure the proper alignment and avoid concentrated contact of the loading platens and test section of the brittle specimen to avoid premature failure due to possible stress concentrators from misalignment.

While dynamic equilibrium is maintained, a ramp incident pulse should be employed to achieve approximate constant strain rate in a brittle specimen that behaves nearly linear elastic until fracture (Duffy et al. 1971; Nemat-Nasser et al. 1991). When the specimen behavior deviates from linear elastic, as encountered in the study of WC–xCo cermets, the profile of the loading pulse needs to be adjusted accordingly. Frew et al. (2002) conducted dynamic experiments on a slightly nonlinear material with a low stiffness and low compressive strength (<500 MPa). The cermet studied in this work is much stiffer and harder. Normally for ceramic materials, the incident pulse is controlled through placing annealed C110 copper wave shapers at the impact end of the incident bar. The plastic deformation of the wave shapers determines how the momentum in the striker is transferred into the incident bar, thereby controlling the time history of the incident pulse. Due to the high strength of WC and the nonlinearity of the stress–strain behavior, annealed copper alone could not produce the required input pulse. In this case, mild steel stacked with annealed copper wave shapers was used to obtain the input pulse to achieve dynamic equilibrium and constant strain rate during the experiments. Furthermore, the length of the incident pulse was controlled by selecting impactors with different lengths so the loading on the specimen stopped shortly after the specimen reached its compressive strength. Thus, only a small portion of the incident pulse is reflected into the incident bar. Most of the momentum from the striker is transmitted through the high-impedance specimen into the transmission bar, which moves the transmission bar away from the specimen before the second compressive pulse in the incident bar (the reflection of the small, reflected pulse from the striking end of the incident bar) reaches the specimen. Therefore, the cermet specimen is loaded only once by a well-recorded loading pulse during one dynamic experiment, facilitating the establishment of the relationship between the loading history and the resultant damage evolution within the microstructural details.

The second modification is aimed at minimizing the stress concentrations in the brittle specimen due to grip rigidity and alignment. One source of stress concentrations is due to the cermet specimen indenting into the steel bar end faces, as the specimen material is harder than the steel bars. To prevent the specimen from indenting into the bars, a pair of laterally confined WC platens (19.1- × 6.35-mm height) were placed between the specimen and bars. The platen technique has been employed by other researchers (Nemat-Nasser et al. 1991; Lankford 1994). The mechanical impedance of the platens used in this research matches that of the bars, minimizing the disturbances caused by the introduction of the platens in the loading axis to the 1-D wave propagations in the bars. A second source of stress concentration could occur from the misalignment of components along the loading axis. Brittle specimens are very sensitive to such misalignment. A slight misalignment will cause the edges of the specimen to be loaded first, creating large local stress concentrations that could lead to premature failure. Unlike quasi-static testing machines that typically have spherical joints for self-alignment, a conventional SHPB does not have such a self-correcting device along its loading axis or gripping system. Therefore, to correct any slight misalignment when a ceramic specimen is under investigation, a simplified spherical joint was placed between the WC platen and the transmission bar (Weerasooriya et al. 2004) as shown schematically in Fig. 2. The joint consisted of a pair of hardened tool steel disks with a spherical joining surface and a curvature of spherical radius of 100 mm in between. The disks have the same diameter as the bars, thus introducing no impedance mismatching to the wave propagation across the interfaces. When assembling the gage section (i.e., the specimen, the platens, and the spherical joint) during an experiment, the pair of spherical surfaces was the last to engage into contact, thus having any angular misalignment automatically corrected. High-vacuum grease was applied between every pair of contacting surfaces along the loading axis to minimize friction.

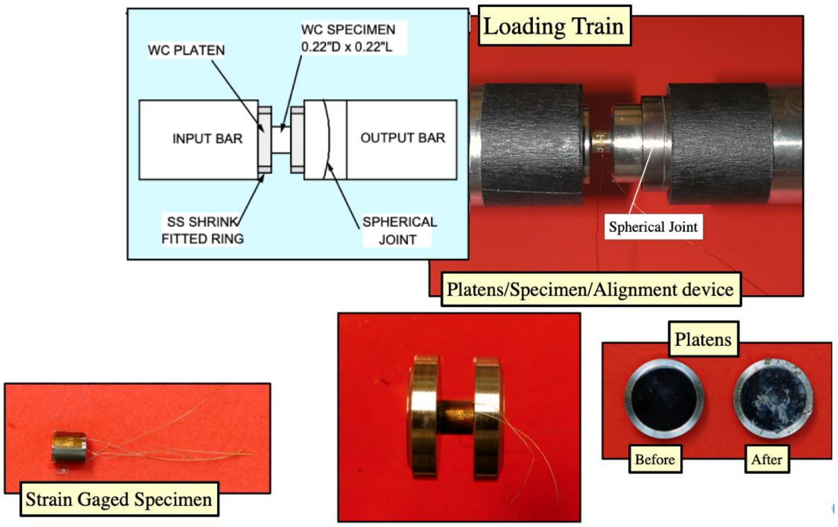

Fig. 2 A schematic (upper left) and photos of high-rate experimental details, clockwise from upper right: details of specimen-bar interface and loading train with hardened tool-steel spherical-coupling, WC platens before and after a typical experiment that are shrink-fitted with stainless-steel collars, specimen with the WC shrink-fitted platens, a typical specimen with the diametrically opposite (180° apart) strain gages

2.4 LR and IR Experimental Method

The LR (0.001/s) and intermediate rate (IR) (1/s) strain experiments were performed using a conventional servo-hydraulically driven Instron testing machine. To align the specimen to the same precision as in the dynamic case, tungsten carbide platens and a spherical joint were also used along the loading axis of the experimental setup. Therefore, the specimen-gripping conditions are the same for the specimen in both quasi-static and dynamic experiments. Figure 3 shows a schematic of the quasi-static setup.

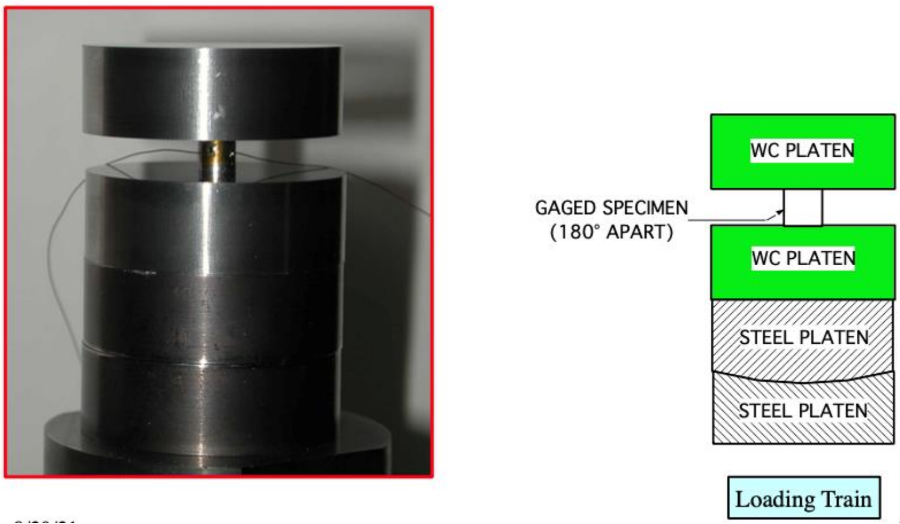

Fig. 3 Photo and schematic of the LR and IR experimental setup showing the loading axis comprising the strain-gaged specimen, WC platens, and spherical steel platens

3. Experimental Results and Discussion

3.1 LR and IR Mechanical Response

3.1.1 Deformation Response

The quasi-static and IR compression experiments were conducted at 0.001/s and 1/s, respectively. The axial load divided by the specimen cross-sectional area was recorded as the stress history in the specimen, whereas the strain measurements were obtained directly from the surface strain gages. The actual strain histories as defined in this work are calculated by averaging the measured signals from the two strain gages mounted 180° apart and an example of the result is shown in Fig. 4. The fact that each individual strain gage data practically overlaps one another indicates that the specimen is evenly loaded during the axial compression, and thus validates the results.

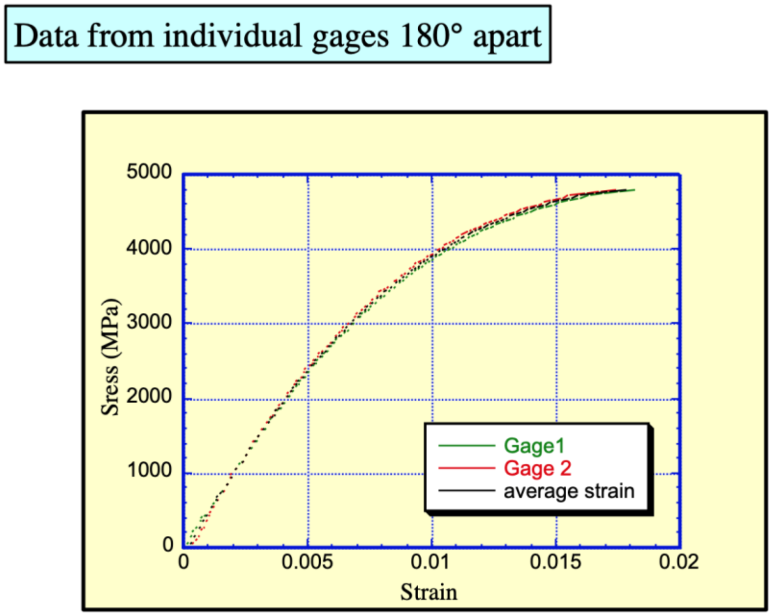

Fig. 4 **A typical set of compressive stress–strain curves obtained from a quasi-static experiment showing the stress strain from two diametrically opposite strain gages, with the stress–strain from the average of the two strain gages indicating precise alignment of the specimen to the loading direction**

The stress–strain curves from slow and intermediate rate experiments for WC–12Co are shown in Fig. 5a. These curves illustrate that the cermet material behaves in a linear elastic manner when the stress is below 2 GPa. Figure 5b shows WC–6Co behaves similarly to WC–12Co. Young's modulus from these portions of the stress–strain curves is estimated to be 538 and 625 GPa for WC–12Co and WC–6Co, respectively. When the axial compressive stress exceeds 2 GPa, the stress–strain curves become nonlinear, which posts a challenge in the follow-up dynamic experiment to maintain a constant strain rate during an experiment. The experiments were repeated under the same experimental conditions for five to six specimens at both 0.001 and 1/s strain rates. Figures 6a and 6b show the effect of the increase of Co content from approximately 6 wt% to 12 wt% for strain rates of 0.001/s and 1/s, respectively. As the Co content is increased, deformation response similarly decreases for both LRs and IRs.

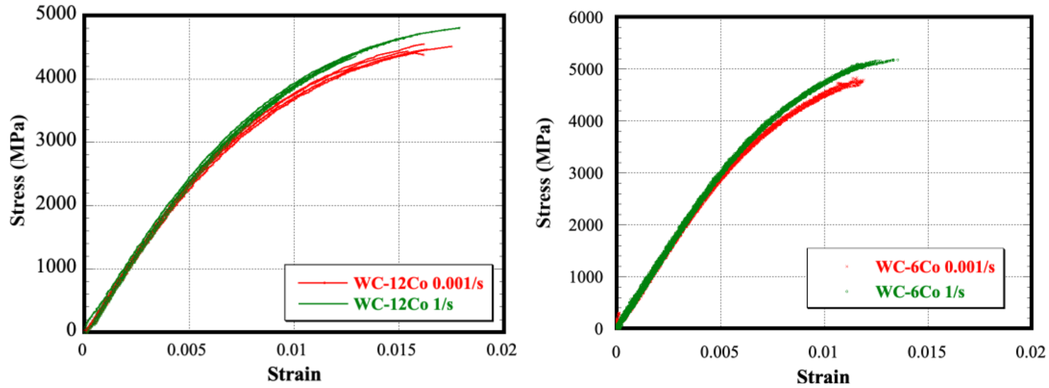

(a) (b)

Fig. 5 Compressive stress–strain behavior at LR and IR strain for (a) WC–12Co and (b) W-6Co

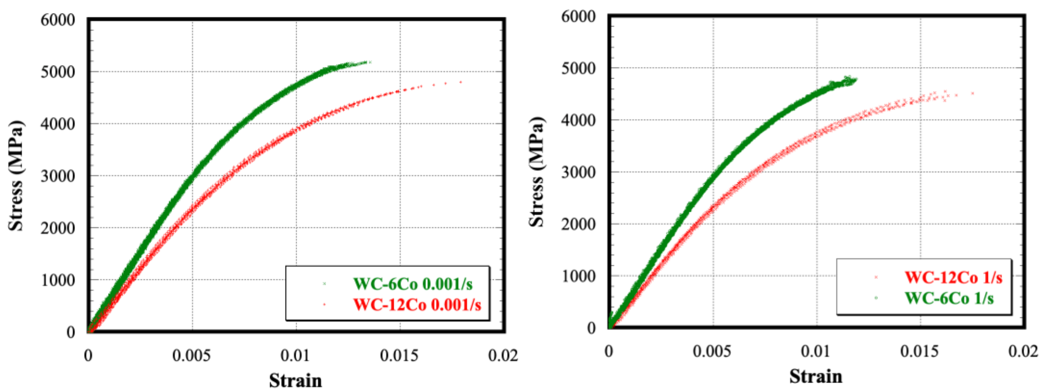

(a) (b)

Fig. 6 Compressive stress–strain response of WC–6Co and WC–12Co at (a) LR and (b) IR strain

3.1.2 Failure Response at LRs and IRs

The failure stresses from these experiments for strain rates of 0.001 and 1/s are tabulated in Tables 2 and 3, respectively. The results show that the failure stresses are very consistent for such brittle materials. At 0.001/s strain rate, the mean compressive strength is 4.469 ±0.052 GPa and 4.766 ±0.054 GPa for WC–12Co and WC–6Co, respectively. At 1/s strain rate, the mean compressive strength rises to 4.694 ±0.067 GPa and 5.110 ±0.052 GPa for WC–12Co and WC–6Co, respectively.

Table 2 Failure stresses WC–12Co and WC–6Co at 0.001/s LR strain

Specimen ID	Failure stress (MPa)	Failure strain	Specimen ID	Failure stress (MPa)	Failure strain
WC12Co-N01	4443	0.0155	WC6Co-C21	4472	0.0117
WC12Co-N02	4414	0.0157	WC6Co-C22	4721	0.0114
WC12Co-N03	4547	0.0162	WC6Co-C23	4764	0.0125
WC12Co-N12	4431	0.0154	WC6Co-C24	4760	0.0120
WC12Co-N13	4464	0.0163	WC6Co-C25	4712	0.0108
WC12Co-N14	4514	0.0175	WC6Co-C26	4864	0.0111
Mean	**4469**	**0.0161**	**Mean**	**4716**	**0.0116**
Std. dev.	**52**	**0.0008**	**Std. dev.**	**131**	**0.0006**

Table 3 Failure stresses WC–12Co and WC–6Co at 1/s IR strain

Specimen ID	Failure stress (MPa)	Failure strain	Specimen ID	Failure stress (MPa)	Failure strain
WC12Co-N04	4618	0.0149	WC6Co-C14	5063	0.0118
WC12Co-N05	4701	0.0159	WC6Co-C15	5149	0.0129
WC12Co-N06	4672	0.0155	WC6Co-C16	5062	0.0123
WC12Co-N08	4801	0.0179	WC6Co-C18	5095	0.0122
WC12Co-N10	4676	0.0156	WC6Co-C19	5179	0.0137
WC12Co-N11	4356	0.0129	WC6Co-C20	5114	0.0121
Mean	**4637**	**0.0155**	**Mean**	**5110**	**0.0125**
Std. dev.	**150**	**0.0016**	**Std. dev.**	**47**	**0.0007**

The results from both sets of experiments at LR and IR strain clearly demonstrate that the compressive response of the WC–xCo cermets depend both on the Co content and strain rate, even within the quasi-static to intermediate range of strain rates. The material lower in Co content exhibits higher compressive strength. The compressive strengths for both cermets are consistently higher at the higher strain rate. Failure stresses as a function of strain rates are summarized and discussed in Section 3.2.3 with the HR failure stresses.

3.2 Dynamic Mechanical Response

Typical oscilloscope records from SHPB experiments on WC–12Co specimens are shown in Fig. 7. The resulting plot shows time histories of the pulses in the incident and transmission bars with the strain histories from the specimen surface strain gages. As shown in Figs. 7a and 7b, the profile of the incident pulse is quite different from that commonly seen in a conventional SHPB experiment. This is the result of careful wave shaping for these experiments. The purpose of creating such a loading pulse is to reach a constant strain rate in the nonlinear specimen. The result of this effort is evident on the reflected signal in Figs. 7a and 7b, which show a nearly constant plateau during the experiment. Since the reflected pulse is proportional to the strain rate in the specimen, an approximate constant strain rate is achieved in the brittle cermet specimen by the wave-shaping technique when the deformation is small. The constant strain rate is also verified by the direct strain-history measurement from the strain-gages on the specimen's surface. The straight ramp signals obtained from the two diametrically opposite strain gages on the specimen have an approximately common slope, which is a direct measurement of the constant strain rate in the specimen. The nearly overlapping strain histories from the specimen strain gages indicate that the specimen deforms nearly uniformly under dynamic equilibrium during the dynamic compressive loading. This indicates the effectiveness of the use of the spherical joint and multi-material platen techniques employed in the dynamic experiments reported here. During HR experiments, strain signals from two gages from the specimen did not completely overlap for all the experiments as in the case of LR experiments. This could be due to a combination of the complexity in the loading train as well as the possible nonuniformity in bonding of adhesives used to adhere the strain gages to the highly polished WC surface, especially during the HR loading. In addition, compared to LR and IR experiments, the fact that the HR loading train is horizontal makes alignment of the specimen to the loading axis more complicated and uncertain. Therefore, during data reduction, strain of the specimen was obtained by averaging the strain measurement of the two gages on the specimen, rather than the traditional use of the reflected pulse of the experiment. Also, note that failure visually initiates after the maximum load is reached (Figs. 7a and 8).

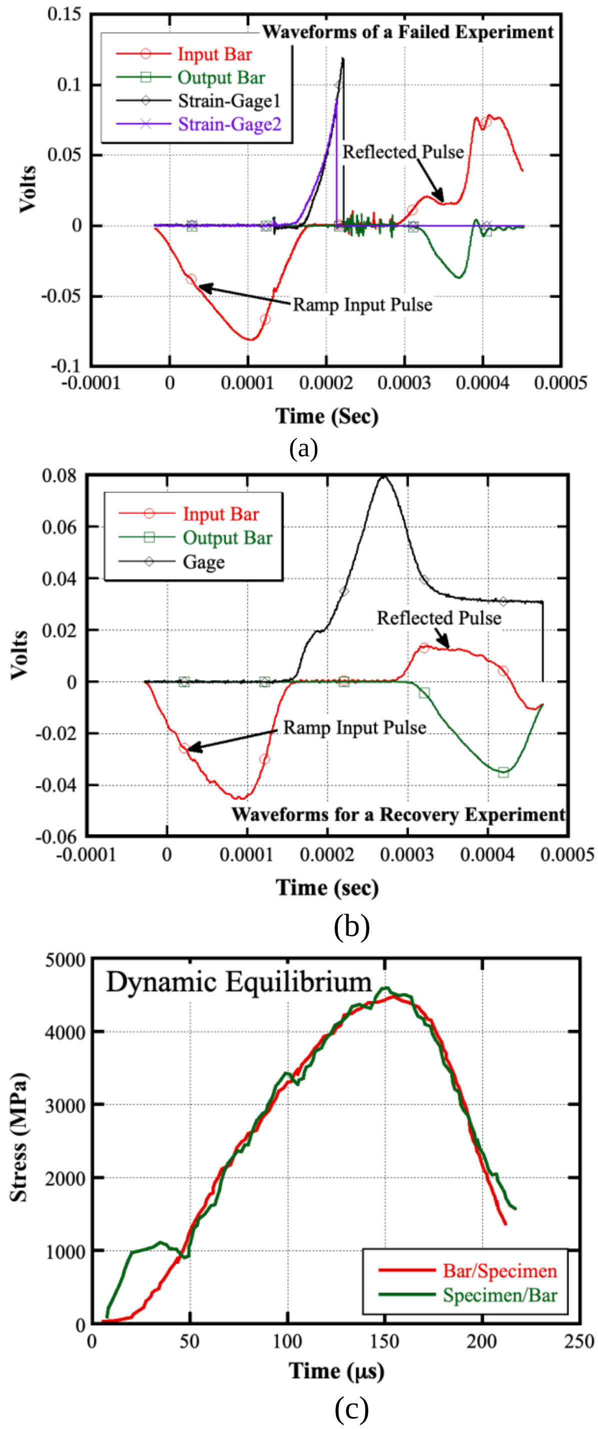

Fig. 7 Wave forms from dynamic split-Hopkinson experiments. (a) Input bar traces for full-failure experiment showing ramp incident wave, and approximately flat reflected wave showing approximate constant strain rate during loading. This plot also shows strain from the diametrically opposite strain gages. (b) Input and output bar strain wave forms for a partially loaded experiment at a loading level below that needed for full failure. (c) Overlapping stress wave forms at both loading bar-specimen interfaces for a typical HR experiment.

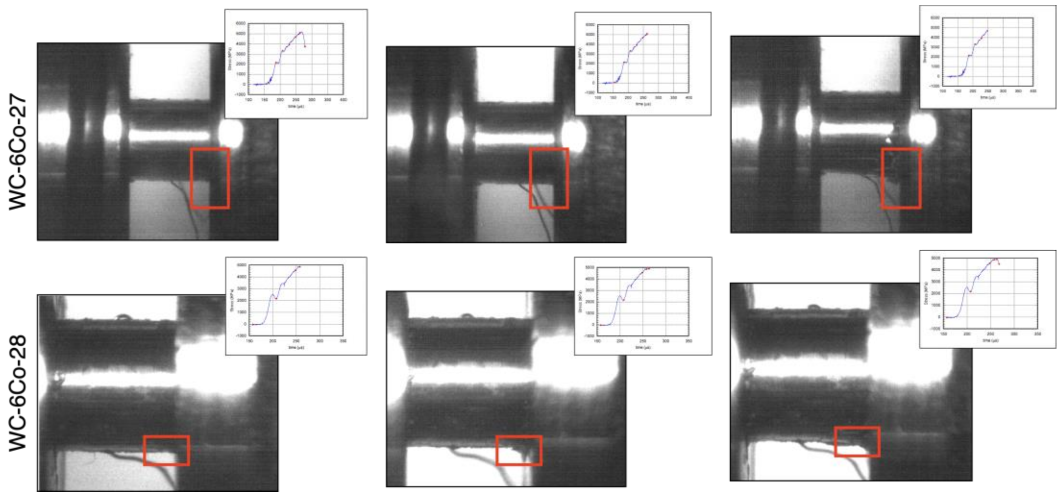

Fig. 8 High-speed photography showing failure initiation after the peak load at the geometric defects at the corner of the specimen

During some of the HR experiments, the specimen was photographed using a high-speed camera to observe the failure process. Figure 8 shows three photos for each of the two specimens (i.e., WC–6Co-27 and WC–6Co-28) with the corresponding load-time trace while failure is initiating. The photo sequence (total of 16 photos for each specimen) shows failure seems to initiate at the constant-stress concentrator, a geometric defect at the corner. Thus, failure stress may differ if the failure initiates at a preexisting critical dominant microstructural defect or other dominant geometric surface defects. We believe the failure stress obtained here could be used as representative values of the failure stress of WC–xCo, as it is unlikely that a failure stress could be measured successfully independent from defects arising from microstructural details. Also, the failure stresses obtained here provide data for studying the effect of different amounts of Co binder in WC on failure, as the same quantifiable magnitude of geometric defect for failure initiation was applicable across the different Co weight percentages.

3.2.1 Dynamic Deformation Response

Stress–strain response at HR for both WC–12Co and WC–6Co are shown in Fig. 9a. Stress strain is almost linear until failure in WC–6Co, whereas for WC–12Co, stress response deviates from linearity due to the increased presence of softer Co in the composite. Stress–strain behavior for all loading rates is summarized in Figs. 9b and 9c for WC–12Co and WC–6Co, respectively. In general, these results show that there is a subtle rate sensitivity as the flow stresses stiffens with the increase in strain rate. WC–6Co response is more linear at HR and stiffer at IR and LR than WC–12Co. This is due to the presence of higher amount of ductile Co phase in WC–12Co compared with WC–6Co. HR experiments have more scatter than LR experiments due to the experimental difficulties using the modified SHPB setup that were discussed in Section 3.2, especially in strain measurements and loading with a complex loading train. These results show there is room for improvement with further development of HR Hopkinson bar experimental methods to reduce experimental variability.

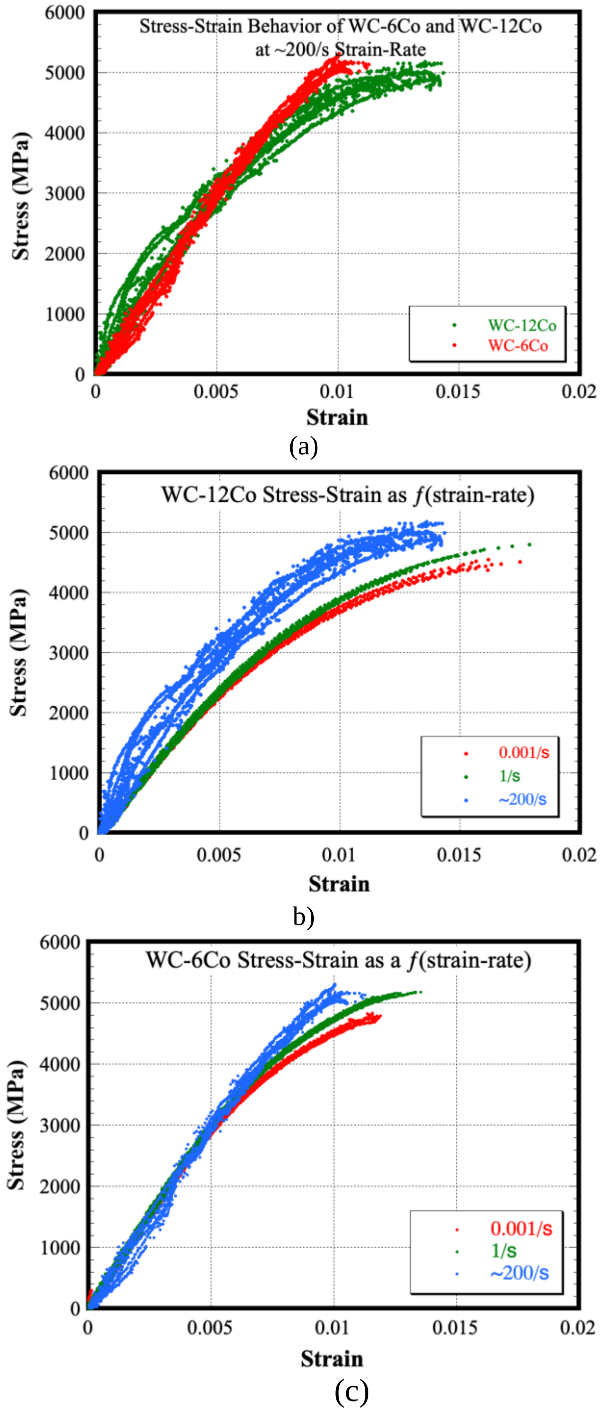

Fig. 9 Stress–strain response (a) at HR for WC–12Co and WC–6Co, and as a function of strain rate for (b) WC–12Co and (c) WC–6Co

3.2.2 Dynamic Failure Response

Measured failure stresses and strains for HR experiments are presented in Table 4. The results show that at a strain rate of approximately 200/s, failure stresses have a mean compressive strength of 4.883 ±0.227 GPa for WC–12Co and 4.638 ±0.672 GPa for WC–6Co. Scatter, as measured by standard deviation, is higher in HR data than in LR data due to additional uncertainties for HR experiments discussed in Section 3.2, even though unique methods were used for alignment.

Table 4 Failure stresses for WC–12Co and WC–6Co at approximately 200/s HR strain rate

Specimen ID	Failure stress (MPa)	Failure strain	Specimen ID	Failure stress (MPa)	Failure strain
WC12Co-C21	4502	0.0156	WC6Co-C01	5106	0.0115
WC12Co-C22	4596	0.0135	WC6Co-C03	5125	0.0103
WC12Co-C23	4918	0.0148	WC6Co-C04	5127	0.0094
WC12Co-C24	4744	0.0153	WC6Co-C06	4664	0.0109
WC12Co-C25	4918	0.0159	WC6Co-C07	4762	0.0127
WC12Co-C26	4744	0.0170	WC6Co-C09	2956	0.0121
WC12Co-C27	5080	0.0160	WC6Co-C11	4455	0.0113
WC12Co-C28	5241	0.0192	WC6Co-C12	4734	0.0107
WC12Co-C29	4986	0.0146	WC6Co-C13	4811	0.0119
WC12Co-C17	5140	0.0130	**Mean**	**4638**	**0.0112**
WC12Co-C18	4846	0.0133	**Std. Dev.**	**672**	**0.0010**
Mean	**4883**	**0.0153**	**Specimen ID**	**Failure stress (MPa)**	**Failure strain**
Std. dev.	**227**	**0.0018**	WC6Co-C01	5106	0.0115

3.2.3 Failure Stress as a Function of Strain Rate

Compressive failure stresses as a function of strain rate obtained from the experiments for both 12Co and 6Co materials are shown in Fig. 10. The results indicate that failure stress generally increases with the strain rate for WC–12Co for strain rates from 0.001 to 200/s. The increase of failure stress with strain rate could be due to the decreased rate of nucleation and mobility of the dislocations at HR leading to requiring an increase in stress required for crack nucleation to initiate failure. As shown in Fig. 10b for WC–6Co, failure stress increases with strain rates up to 1/s but decreases as the strain rate reaches 200/s. We are uncertain about the reason for this apparent decrease. This decrease could either be due to material behavior or the experimental difficulties and uncertainties associated with characterizing highly brittle materials at HRs, since WC–6Co was more brittle than WC–12Co. For example, since WC–6Co is inherently brittle, it may have had a higher possibility of the failure crack nucleating at a stress concentration due to any slight misalignment in the corner even though we use a novel alignment technique.

These uncertainties were further exaggerated for WC–0Co experiments at HRs (Appendix). Figure 10c directly compares the failure stress for the two different Co weight percentages. The average strength of the alloy increased as the relative amount of Co content decreased. This inverse relationship between Co content and failure strength was due to the ductility and lower strength of Co compared with WC, just as the greater ductility of Co was also responsible for the more linear behavior of the stress–strain response of the lower Co cermet at the same strain rate (see Figs. 6 and 9a).

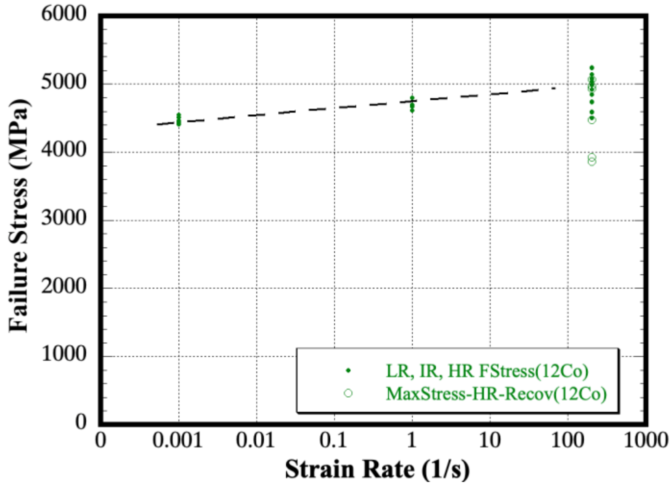

(a)

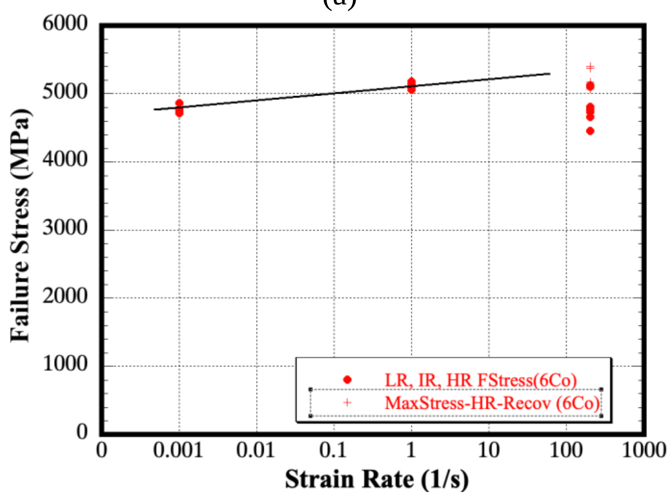

(b)

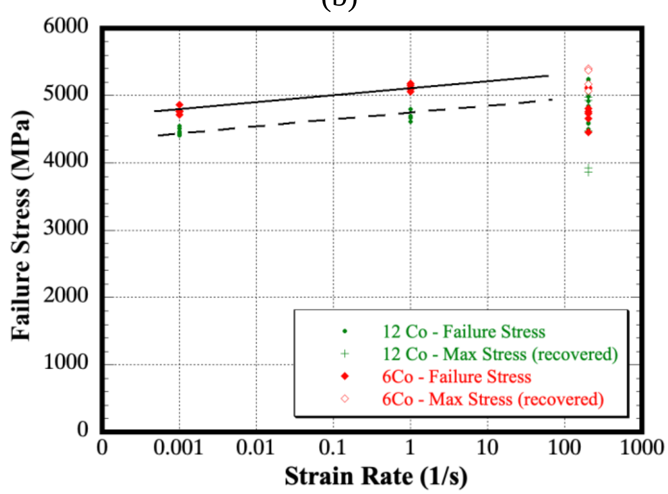

(c)

Fig. 10 Failure stress as a function of strain rate for (a) WC–12Co, (b) WC–6Co, and (c) both WC–12Co and WC–6Co

The failure-stress data in Fig. 10 (excluding 200/s WC–6Co data) can be correlated with the strain rate by using either a power law or a logarithmic law. The two forms of representation of failure-stress–strain-rate relationship are

$$\sigma = A \cdot \text{MPa} \quad (1)$$

$$\sigma = B + 78.31 \cdot log\text{MPa}, \quad (2)$$

where A is 4695 MPa for WC–12Co and 5024 MPa for WC–6Co, and B is 4701 MPa for WC–12Co and 5030 MPa for WC–6Co. These relationships can be used to represent the failure behavior of these cermets (excluding HR 200/s behavior for WC–6Co).

3.3 Initiation of Damage from Recovered Specimens

Some of the HR experiments were designed and performed to investigate the microstructural process of damage initiation and propagation in the specimens. Specimens were recovered at different points along the loading curve by controlling the input pulse so the magnitude of loading strain was lower than the average failure strain of the specimens. The specimens that were recovered at different magnitudes of applied strains were then polished and examined under an optical microscope. We were able to observe cracks in only two of the recovered WC–12Co specimens out of all the recovered 6Co and 12Co cermets. The crack had already propagated beyond the initiation point because the time between initiation of the cracks and the catastrophic failure is very short for WC cermet materials, even with higher ductile 12Co. Therefore, we were not able to stop at the precise moment of crack nucleation to identify experimentally how the crack nucleates in these two different cermets. Figure 11 shows a cross section of the recovered damaged WC–12Co specimen. The image shows that the failure initiates from the surface and predominantly follows an intergranular path. Two cracks emanate from the surface, but one crack dominates the damage process. Recovery was attempted on only a few HR experiments due to the enormous complexity of conducting recovery experiments. This methodology requires loading specimens and subsequently unloading at predetermined loads below the catastrophic average failure threshold, followed by the laborious process of searching for damage through microstructural analysis.

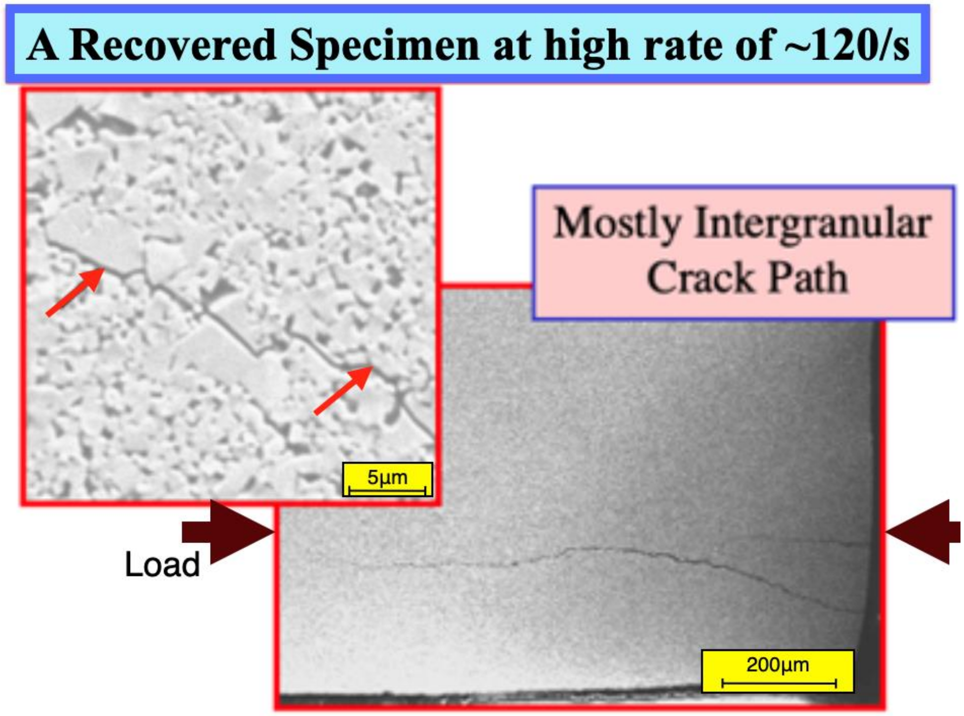

Fig. 11 Sectioned and polished HR WC–12Co unloaded recovered specimen before complete failure, with a known load-time history

4. Conclusions

The deformation and failure responses of WC–12Co and WC–6Co have been determined as a function of loading rates from low (quasi-static), through intermediate, to dynamic strain rates. Unique capabilities were employed for these experiments. To determine the dynamic properties, a SHPB modified with wave shaping and a spherical joint is employed. A similar spherical joint is used in the LR and IR experiments to minimize stress concentrations in the specimen through precise alignment. The results show that the compressive stress–strain behaviors of the cermets are slightly nonlinear, with the nonlinearity increasing with Co content. Failure strengths are sensitive to both Co contents and strain rates: average LR, IR, and HR strengths for WC–6Co were 4.8, 5.1, and 4.6 GPa, respectively; for WC–12Co they were 4.5, 4.7, and 4.9 GPa, respectively. The rate dependency is quantitatively summarized by two rate-dependent failure models. Optical micrographs from recovered specimens indicated that damage propagation during deformation is predominantly intergranular.

5. References

Alexander S, Weerasooriya T. Mechanical characterization of advanced ultra-high molecular weight polyethylene (UHWMPE) composites by ultrasonic method. DEVCOM Army Research Laboratory (US); 2021 Aug. Report No.: ARL-TR-9254. https://apps.dtic.mil/sti/pdfs/AD1146645.pdf.

Anton RJ, Subhash G. Dynamic Vickers indentation of brittle materials. Wear. 2000;239(1):27–35.

Brown AD, Rafaels KA, Weerasooriya T. Shear behavior of human skull bones. J Mech Behav Biomed Mater. 2021;116:104343. doi:10.1016/j.jmbbm.2021.104343.

Chen W, Ravichandran G. Static and dynamic compressive behavior of aluminum nitride under moderate confinement. J Am Ceramic Soc. 1996;79(3):579–584.

Chen W, Ravichandran G. Dynamic compressive behavior of a glass ceramic under lateral confinement. J Mech Phys Solids. 1997;45(8):1303–1328.

Chen W, Song B. Split Hopkinson (Kolsky) bar design, testing, and applications. Springer; 2011.

Cheng M. Chen W, Weerasooriya T. Experimental investigation of the transverse mechanical properties of a single Kevlar® KM2 fiber. Int J Solids Struct. 2004; 41(22–23):6215–6232

Cheng M, Chen W, Weerasooriya T. Mechanical behavior of bovine tendon with stress-softening and loading-rate effects. Adv Theor Appl Mech. 2009;2(2):59–74. http://www.m-hikari.com/atam/atam2009/atam1-4-2009/chenATAM1-4-2009.pdf.

Cutler RA. Influence of microstructure on mechanical properties in cemented tungsten carbides [dissertation]. University of Utah; 1984.

Duffy J, Campbell JD, Hawley RH. On the use of a torsional split Hopkinson bar to study rate effects in 1100-0 aluminum. ASME J Appl Mech. 1971;37:83–91.

Favrot N, Besson J, Colin C, Delannay F. Cold compaction and solid-state sintering of WC–Co-based structures: experiments and modeling. J Am Ceramic Soc. 1999;82(5):1153–1161.

Frew DJ, Forrestal MJ, Chen W. Pulse-shaping techniques for testing brittle materials with a split Hopkinson pressure bar. Exp Mech. 2002;42(1):93–106.

Gooch WA, Burkins MS, Palicka R. Ballistic development of US high density tungsten carbide ceramics. J Phys IV. 2000;10(P9):741–746.

Gray GT. Classic split-Hopkinson pressure bar technique. In: Kuhn H, Medlin D, editors. ASM handbook 8: mechanical testing and evaluation. ASM International; 2000.

Kolsky H. An investigation of the mechanical properties of materials at very high rates of loading. Proc Roy Soc London B. 1949;62:676–700.

Lankford JJ. Utilization of the split Hopkinson pressure bar under hydrostatic confining pressure to characterize the compressive behavior of ceramics and ceramic composites. In: Gilat A, editor. Mechanical testing of ceramics and ceramic composites. American Society of Mechanical Engineers; 1994. p. 1–11.

Lee HR, Kim DJ, Hwang NM, Kim D-Y. Role of vanadium additive during sintering of WC–Co: mechanism of grain growth inhibition. J Am Ceramic Soc. 2003;86:152–154.

Luo H, Chen W. Dynamic compressive response of intact and damaged AD995 alumina. Inter J Appl Ceram Tech. 2004;1(3):254–260. doi: 10.1016/j.ijsolstr.2004.05.016.

Moy P, Gunnarsson CA, Weerasooriya T, Chen W. Stress–strain response of PMMA as a function of strain-rate and temperature. In: Proulx T, editors. Dynamic behavior of materials. Conference Proceedings of the Society for Experimental Mechanics Series. Springer; 2011. p. 125–133. doi:10.1007/978-1-4614-0216-9_18.

Nemat-Nasser S, Issacs JB, Starrett JE. Hopkinson techniques for dynamic recovery experiments. Proc Roy Soc London A. 1991;435:371–391.

Peng Z, Miao H, Qi L, Yang S, Liu C. Wear-resistant titanium carbonitride coatings onto WC–Co cutting tools by pulsed high-energy density plasma. J Am Ceramic Soc. 2005;88:1786–1791.

Peron PF. Ballistic development of tungsten carbide ceramics for armor applications. Ceram Trans. 2002;134:45–52.

Ross CA, Jerome DM, Tedesco JW, Hughes ML. Moisture and strain rate effects on concrete strength. ACI Mater J. 1996;93:293–300.

Sanborn B, Gunnarsson CA, Foster M, Weerasooriya T. Quantitative visualization of human cortical bone mechanical response: studies on the anisotropic compressive response and fracture behavior as a function of loading rate. Exp Mech. 2016;56:81–95. doi:10.1007/s11340-015-0060-y.

Schneider S. Engineered materials handbook volume 4: ceramics and glasses. American Society for Materials International; 1991.

Song B, Chen W, Weerasooriya T. Quasi-static and dynamic compressive behaviors of a glass/epoxy composite. J Compos Mater. 2003;37(19):1723–1743.

Song B, Chen W, Ge Y, Weerasooriya T. Dynamic and quasi-static compressive response of porcine muscle. J Biomech. 2007;40(13):2999–3005. doi:10.1016/j.jbiomech.2007.02.001.

Weerasooriya T, Moy P, Chen W. Effect of strain-rate on the deformation and failure of WC–12Co. Paper presented at: 28th International Conference on Advanced Ceramics and Composites; 2004 Jan 25–30; Cocoa Beach, FL.

Weerasooriya T, Sanborn B, Gunnarsson CA, Foster M. Orientation dependent compressive response of human femoral cortical bone as a function of strain rate. J Dyn Behav Mater. 2016;2:74–90. doi:10.1007/s40870-016-0048-4.

Appendix. Failure Stresses from Each Experiment at Different Strain Rates for WC–xCo

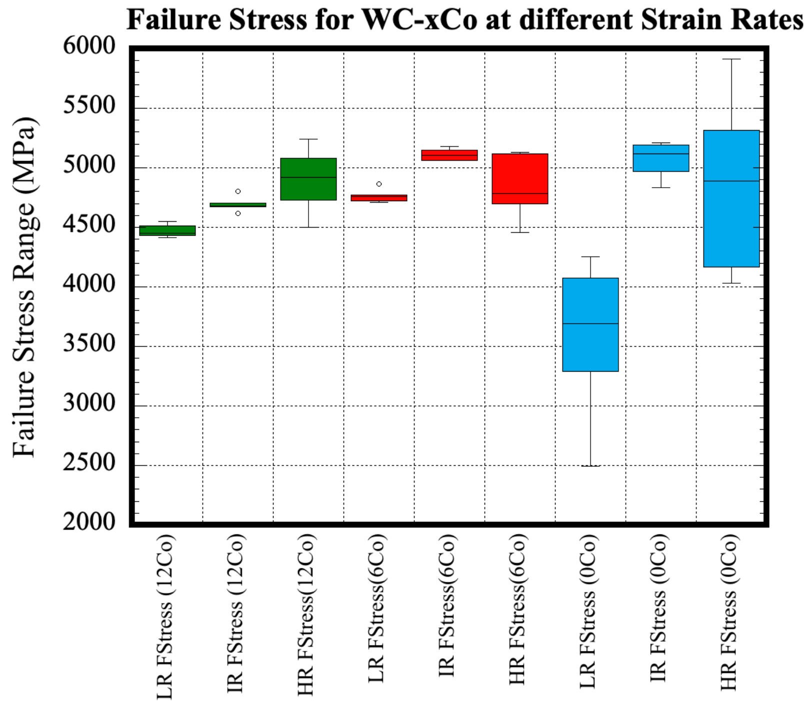

Fig. A-1 Box plot of failure-stress distribution at low rate (LR), intermediate rate (IR), and high rate (HR) for WC–12Co, WC–6Co, and WC–0Co

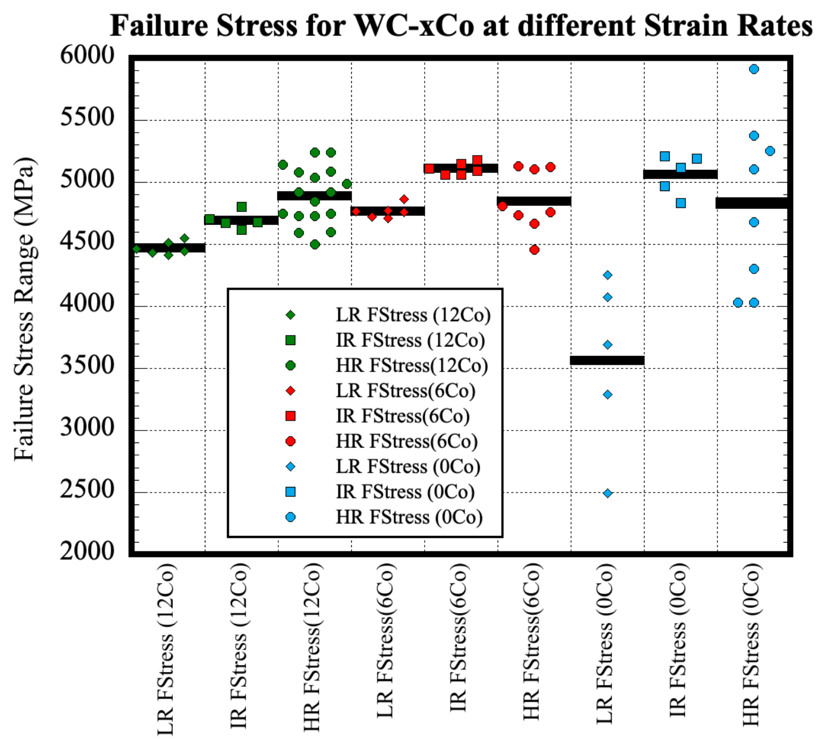

Fig. A-2 Dot plot of individual failure-stress magnitudes at LR, IR, and HR for WC–12Co, WC–6Co, and WC–0Co

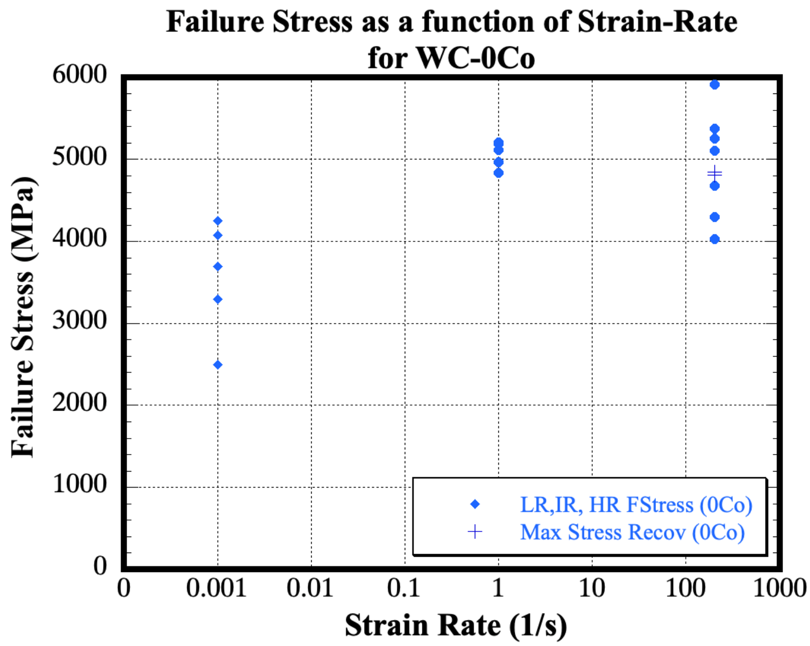

Fig. A-3 Failure stress as a function of LR, IR, and HR for WC–12Co, WC–6Co, and WC–0Co

List of Symbols, Abbreviations, and Acronyms

1-D	one-dimensional
ARL	Army Research Laboratory
Co	cobalt
DEVCOM	US Army Combat Capabilities Development Command
HR	high rate
ID	identification
IR	intermediate rate
LR	low rate
SEM	scanning electron microscope
SHPB	split-Hopkinson pressure bar
WC	tungsten carbide
WC–xCo	WC with "x" wt% Co

1 DEFENSE TECHNICAL
(PDF) INFORMATION CTR
DTIC OCA

1 DEVCOM ARL
(PDF) FCDD RLB CI
TECH LIB

11 DEVCOM SC
(PDF) MG CARBONI
D COLANTO
R DILLALLA
B FASEL
J FONTECCHIO
B KIMBALL
J KIREJCZYK
J PARKER
M MAFEO
M MARKEY
D PHELPS

3 PEO SOLDIER
(PDF) J HOPPING
J MULLENIX
D OTTERSON

1 PEO IEWS
(PDF) A FOURNIER

1 MTRL SCIENCES DIV
(PDF) LAWRENCE BERKELY
NATL LAB
R RITCHIE

5 SOUTHWEST RSRCH INST
(PDF) C ANDERSON JR
S CHOCRON
D NICOLELLA
T HOLMQUIST
G JOHNSON

2 NIST
(PDF) A FORSTER
M VANLANDINGHAM

1 INST FOR DEFNS ANLYS
(PDF) Y MACHERET

3 MRMC DOD BLAST INJURY
(PDF) RSRCH PROGRAM COOR OFC
R GUPTA
T PIEHLER
R SHOGE

2 MRMC JTAPIC PRGM OFC
(PDF) W LEI
J USCILOWICZ

4 US ARMY AEROMEDICAL
(PDF) RSRCH LAB
F BROZOSKI
V CHANCEY
B MCENTYRE
D WISE

1 DEVCOM GVSC
(PDF) R SCHERER

1 DEVCOM C5ISR
(PDF) AMSRD PE
D RUSIN

2 DEVCOM CBC
(PDF) M HORSMON
N VINCELLI

1 OSD DOT&E
(PDF) J IVANCIK

5 US NAVAL RSRCH LAB
(PDF) A BAGCHI
A ILIOPOULOS
J MICHOPOULOS
K TEFERRA
X TAN

4 DAC
(PDF) FCDD DAG S
K LOFTIS
FCDD DAS LBW
G DIETRICH
FCDD DAS LBE
J GURGANUS
S SNEAD

93 DEVCOM ARL
(PDF) FCDD RLA A
S KARNA
A RAWLETT
S SCHOENFELD
FCDD RLA B
M TSCHOPP
A WEST
FCDD RLA CB
R BECKER
J CAMPBELL
P GILLICH
C HOPPEL
A TONGE
J LASALVIA
FCDD RLA HC
A EIDSMORE

A DAGRO
T THOMAS
FCDD RLA M
R BRENNAN
B CHEESEMAN
K CHO
FCDD RLA MA
K BERNETICH
T BOGETTI
S BOYD
J CAIN
M NEBLETT
E SANDOZ-ROSADO
J SANDS
J STANISZEWSKI
M YEAGER
FCDD RLA MB
G GAZONAS
P MOY
D O'BRIEN
J SIETINS
T WALTER
FCDD RLA MC
R JENSEN
FCDD RLA MD
A BUJANDA
E WETZEL
J LA SCALA
FCDD RLA ME
P PATEL
J SWAB
L VARGAS-GONZALEZ
FCDD RLA MF
K DARLING
S GRENDAHL
C HAINES
H MURDOCH
FCDD RLA MG
J LENHART
R MROZEK
FCDD RLA T
R FRANCART
FCDD RLA TA
S BILYK
FCDD RLA TB
S ALEXANDER
T BAUMER
A BROWN
B FAGAN
A GOERTZ
A GUNNARSSON
C HAMPTON
M KLEINBERGER
E MATHEIS
J MCDONALD
P MCKEE
K RAFAELS
S SATAPATHY
M TEGTMEYER
T WEERASOORIYA
S WOZNIAK
T ZHANG
D CASEM
J CLAYTON
C MEREDITH
L SHANNAHAN
T PLAISTED
FCDD RLA TD
R DONEY
R GUPTA
B KRZEWINSKI
K MASSER
F MURPHY
C RANDOW
M ZELLNER
FCDD RLA TE
J LLOYD
M LOVE
P SWOBODA
FCDD RLA TF
J CAZAMIAS
T EHLERS
L MAGNESS
CS MEYER
FCDD RLA TG
N GNIAZDOWSKI
S KUKUCK
FCDD RLA V
S SILTON
FCDD RLA VA
R EMERSON
FCDD RLA VB
A HALL
FCDD RLA W
TV SHEPPARD
FCDD RLA WE
TG BROWN
FCDD RLB
J ZABINSKI
FCDD RLD
FCDD RLD M
N ZANDER
FCDD RLW V
FCDD RLR A
D STEPP
FCDD RLR EW
R ANTHENIEN

UNIVERSITIES/INDUSTRY

4 (PDF) WHITING SCHOOL OF ENG
JOHNS HOPKINS UNIV
S BAILOOR
T D NGUYEN
B NOTGHI
KT RAMESH

5 (PDF) GEORGIA INST OF TECH
S KALIDINDI
S MARGULIES
D MCDOWELL
N THADHANI
M ZHOU

1 (PDF) DEPT OF ENGRNG SCI AND MECHANICS
VIRGINIA POLYTECHNIC INST AND STATE UNIV
R BATRA

4 (PDF) MASSACHUSETTS INST OF TECHLGY
INST FOR SOLDIER NANOTECHNOLOGIES
M J BUEHLER
R RADOVITZKY
C SCHUH
S SOCRATE

1 (PDF) DEPT OF MECHL AND NUCLEAR ENGRNG
THE PENNSYLVANIA STATE UNIV
R KRAFT

1 (PDF) INDIAN INST OF TECH
R BHARDWAJ

2 (PDF) CENTER FOR APPLIED BIOMECHANICS
UNIV OF VIRGINIA
MB PANZER
R SALZAR

1 (PDF) UCSD MAT SCI AND ENG
M MEYERS

1 (PDF) DUKE UNIV
BIOMED ENG
CR BASS

1 (PDF) UNIV OF CAPE TOWN
BLAST IMPACT & SURVIVABILITY UNIT
TJ CLOETE

1 (PDF) UNIV OF OXFORD
BLAST IMPACT & SURVIVABILITY UNIT
C SIVIOUR

2 (PDF) UNIV OF CAMBRIDGE
ENG DEPT
V DESHPANDE
B LIU

4 (PDF) UNIV OF SOUTH CAROLINA
COL OF ENG
S RAJAN
S SOCKALINGAM
M SUTTON
F THOMAS

1 (PDF) IMPERIAL COL LONDON
DEPT OF PHYSICS
W PROUD

1 (PDF) DIV OF ENG AND APPL SCI
CALTECH
R RAVICHANDRAN

1 (PDF) DEPT OF AERO ENG AND ENG MECH
U TEXAS AUSTIN
K RAVI-CHANDAR

1 (PDF) AERO AND ASTRO ENG
PURDUE UNIV
W CHEN

1 (PDF) DEPT OF NEUROSURGERY
MED COL OF WISCONSIN
N YOGANANDAN